Power Reserve Control of PV Grid-Tied Inverter With Transient Stability Constraint

Yangjian Ling, Meng Huang, *Member, IEEE*, Pan Feng, Minxuan Peng, *Graduate Student Member, IEEE*, Zhen Tian, *Member, IEEE*, Sirui Shu, Xiaoming Zha, *Senior Member, IEEE*, and Xin Ma

***Abstract*—To support the grid frequency, the power reserve control is adopted in the photovoltaic (PV) system without the energy storage. As an important part of the PV system, the influence of the dc-link voltage dynamics is ignored in the grid-tied inverter so that the PV source and grid-tied inverter cooperative control is rarely designed to enhance the transient stability. In this article, the dc-link voltage dynamics are taken into consideration for the transient stability analysis of the grid-following (GFL) control and the grid-forming (GFM) control. It is found that the dc-link voltage dynamics deteriorate the transient stability of the GFL inverter and the GFM inverter. By analogy with the mass-spring-damper system, the enhanced controls are proposed with the equivalent elasticity for the GFL inverter and the GFM inverter. To support the grid frequency and enhance the transient stability, the frequency deviation feedback and equivalent elasticity cooperative control is proposed to regulate the active power of the PV source. Simulation tests are performed on a 10 kW grid-tied PV system and experimental tests are performed on a 1500 W grid-tied PV system, where the effectiveness of enhanced controls is verified.**

***Index Terms*—Frequency support, grid-following control, grid-forming control, power reserve control, transient stability.**

NOMENCLATURE

List of Abbreviations

PV	Photovoltaic.
GFL	Grid-following.
GFM	Grid-forming.
PLL	Phase-locked loop.
RES	Renewable energy source.
LOS	Loss of synchronization.
EAC	Equal area criterion.
SGs	Synchronous generators.
VSG	Virtual synchronous generator.
PCC	Point of common coupling.

List of Symbols

P	Active power.
α	Power reserved factor.
V_{dc}	Dc-link voltage.
V_{g}	Grid voltage.
L_{g}	Grid inductance.
C_{dc}	Dc-link capacitor.
ω_{PLL}	Frequency of PLL.
ω_{VSG}	Frequency of VSG.
I_{t}	Output current of grid-tied inverter.
V_{t}	PCC voltage.
θ_{g}	Phase angle of V_{g}.
θ_{PLL}	Phase angle of PLL.
θ_{VSG}	Phase angle of VSG.
δ_1	Angle difference between θ_{PLL} and θ_{g}.
δ_2	Angle difference between θ_{VSG} and θ_{g}.
k_{ppv}	Proportional gain of dc-link voltage loop for GFL.
k_{piv}	Integral gain of dc-link voltage loop for GFL.
k_p	Proportional gain of PLL.
k_i	Integral gain of PLL.
k_{pv}	Proportional gain of dc-link voltage loop for GFM.
k_{iv}	Integral gain of dc-link voltage loop for GFM.
J	Virtual inertia.
D_p	Virtual damping.
k_Q	Reactive power droop coefficient.
$k_{\mathrm{e}1}$	Equivalent elastic coefficient of GFL.
$k_{\mathrm{w}1}$	Frequency feedback coefficient of GFL.
$k_{\mathrm{e}2}$	Equivalent elastic coefficient of GFM.
$k_{\mathrm{w}2}$	Frequency feedback coefficient of GFM.

List of Subscripts

d, q	Index on the dq-frame.
0	Rated value

I. INTRODUCTION

RECENTLY, the RES penetration increases fast in the power grid. Traditional power grid is turning to be the power electronics dominated power system. Massive voltage source inverters are adopted to connect the PV source or the wind power to the power grid. And the RES should support the grid voltage and the frequency under grid disturbances.

Usually, the PV source operates at the maximum power point to achieve higher efficiency. However, it makes the PV source unavailable for grid supporting. Installing the energy storage can provide extra power to support the grid frequency, but it increases

Received 14 September 2024; revised 29 December 2024 and 8 March 2025; accepted 6 April 2025. Date of publication 15 April 2025; date of current version 30 June 2025. This work was supported by the Science and Technology Project of State Grid Corporation of China under Grant 4000-202399470A-3-2-ZN. Recommended for publication by Associate Editor J. Lam. *(Corresponding author: Meng Huang.)*

Yangjian Ling, Meng Huang, Pan Feng, Minxuan Peng, Zhen Tian, Sirui Shu, and Xiaoming Zha are with the School of Electrical Engineering and Automation, Wuhan University, Wuhan 430072, China, and also with the Hubei Key Laboratory of Power Equipment and System Security for Integrated Energy, Wuhan University, Wuhan 430072, China (e-mail: meng.huang@whu.edu.cn).

Xin Ma is with the Power Research Institute of State Grid Ningxia Electric Power Company Ltd., Yinchuan 750011, China (e-mail: 21610036@zju.edu.cn).

Color versions of one or more figures in this article are available at https://doi.org/10.1109/TPEL.2025.3560995.

Digital Object Identifier 10.1109/TPEL.2025.3560995

the system cost and complexity. Another widely adopted method is to use the power reserve control in such applications [1], [2], without modifying any hardware on the existing installed PV inverters. With the power reserve control, the PV source operates at a certain power level lower than the maximum power point. The extra power can be provided to support the power grid.

Existing power reserve controls are proposed to improve the performance of the PV grid-tied system [3], [4]. The partial shading conditions are considered to design the new control and estimate the maximum available power to support the grid [5], [6]. However, these methods are focusing on the control of power level and neglecting the stability issues during the transient disturbances. At present, the GFL control is widely used in the PV system due to its simple control. However, the GFL inverter would lose stability under the weak grid [7]. To adapt to the weak grid and support the grid voltage, the GFM inverter is applied in the RES system [8]. Both of the GFL inverter and the GFM inverter are threatened by disturbances like grid voltage drops [9]. In 2017, the current injection is ceased when the grid voltage is lower than 0.9 per unit. It causes a large-scale PV source tripping event in southern California [10]. In 2021, the grid voltage drop causes the large phase angle deviation of the PLL, the inverters issue a fault code and shut down, which results a large-scale PV source tripping event in Odessa [11]. The events are partially caused by the LOS between the PV source and the power grid [12], [13]. Therefore, the transient stability constraint should be considered when performing the power regulation in such controls. To analyze the transient stability of the grid-tied inverter, the phase portrait is introduced in [14] and [15]. To reveal the mechanism of transient instability, the EAC is applied due to the similarity between SGs and the PLL [16]. There is a risk of the negative damping which deteriorates the transient stability [17]. To evaluate the influence of the varying damping, an iterative EAC is proposed for transient stability analysis in [18] and an energy function is applied to analyze the influence of the damping in [19]. The time-domain expression of the PLL is derived with the averaging method in [20], and the stability criterion is proposed and the influences of control parameters and grid impedance are analyzed. However, in these stability studies, the dc-link dynamics are neglected and the input power of grid-tied inverter is simplified as a constant. This is not practical in the power reserve control since the active power of the PV source can be regulated at different levels under various grid conditions.

Actually, the power reserve control provides a possibility of stability enhancement during the transient, besides its grid supporting capability. Traditionally, to improve the transient stability, enhancement methods are proposed for the control loops of grid-tied inverter. An enhanced PLL based on the additional damping is adopted in [21]. Similarly, an additional damping is designed through feeding back the frequency deviation of the PLL in [22]. High-pass filters are added to avoid the steady-state offset of the frequency deviation and can provide extra damping under different grid voltage drops. Since the integral gain of the PLL is negative for the damping, the integral regulator is removed once the grid fault occurs [23]. To improve the transient stability and the phase-tracking accuracy, the integral regulator is frozen when the rate-of-change-of-frequency of the PLL is larger than a value [24]. The frequency deviation between the PLL and the VSG is fed back to increase the damping in [25]. The transient stability of the GFM inverter is improved by using adaptive inertia and damping control [26]. To regulate the active power reference of the RES, the inertia synchronization control is proposed in [27]. In above studies, the transient stability is designed well, but the dc-link dynamics are rarely considered.

To improve the stability of power reserve control and enhance the transient performance of the PV grid-tied inverter, the power reserve control with transient stability constraint is proposed in this article. The influence of the dc-link dynamics on the transient stability is taken into consideration with the EAC method. The enhanced controls of the GFL inverter and the GFM inverter are proposed to improve the transient stability. The rest of this article is organized as follows. The PV grid-tied system is described and the models of the GFL control and the GFM control are built in Section II. The influences of the reactive power and the dc-link dynamics on the transient stability are analyzed in Section III. The frequency deviation feedback and equivalent elasticity cooperative controls are proposed to enhance power reserve control in Section IV. Simulations and experiments are displayed in Section V to verify the effectiveness of the enhanced controls. Finally, Section VI concludes this article.

II. SYSTEM DESCRIPTION AND MODELING

A. *System Description*

The structures of the GFL inverter and the GFM inverter are shown in Fig. 1. The PV grid-tied system outputs a constant power with the power reserve control. The dc–dc part is a boost converter. The power control is applied to calculate the duty cycle. The power reference is P_0, which is lower than the maximum power $P_{\max}$. P_0 is in the range of [0, $P_{\max}$]. ΔP is the reserved power, which can support the grid frequency. V_{dc} is controlled by the dc-link voltage loop in the grid side inverter. L_{f} is the filter inductance and C_{f} is the filter capacitor. I_{dref} and I_{qref} separately denote the active current reference and the reactive current reference. V_{dc0} is the rated dc-link voltage. The system main parameters are listed in Table I.

To remain stable, the operation point is allocated at the right-hand side of maximum power point [28]. The reserved power is

$$\Delta P = \alpha P_{\max} = \frac{\alpha}{1-\alpha} P_0. \tag{1}$$

B. *Grid-Following Control*

As shown in Fig. 1(a), the active current reference I_{dref} is given by the dc-link voltage loop. During the normal operation, the reactive current reference I_{qref} is set to zero. To provide the ability of the low-voltage ride-through, according to Chinese standard [29], I_{qref} is set to $-K(0.9 - V_{\mathrm{tabc}})I_0$ when V_{tabc} is lower than 0.9 p.u. V_{tabc} is the per unit value of the PCC voltage and I_0 is the rated active current. K is the proportional coefficient of the reactive current.

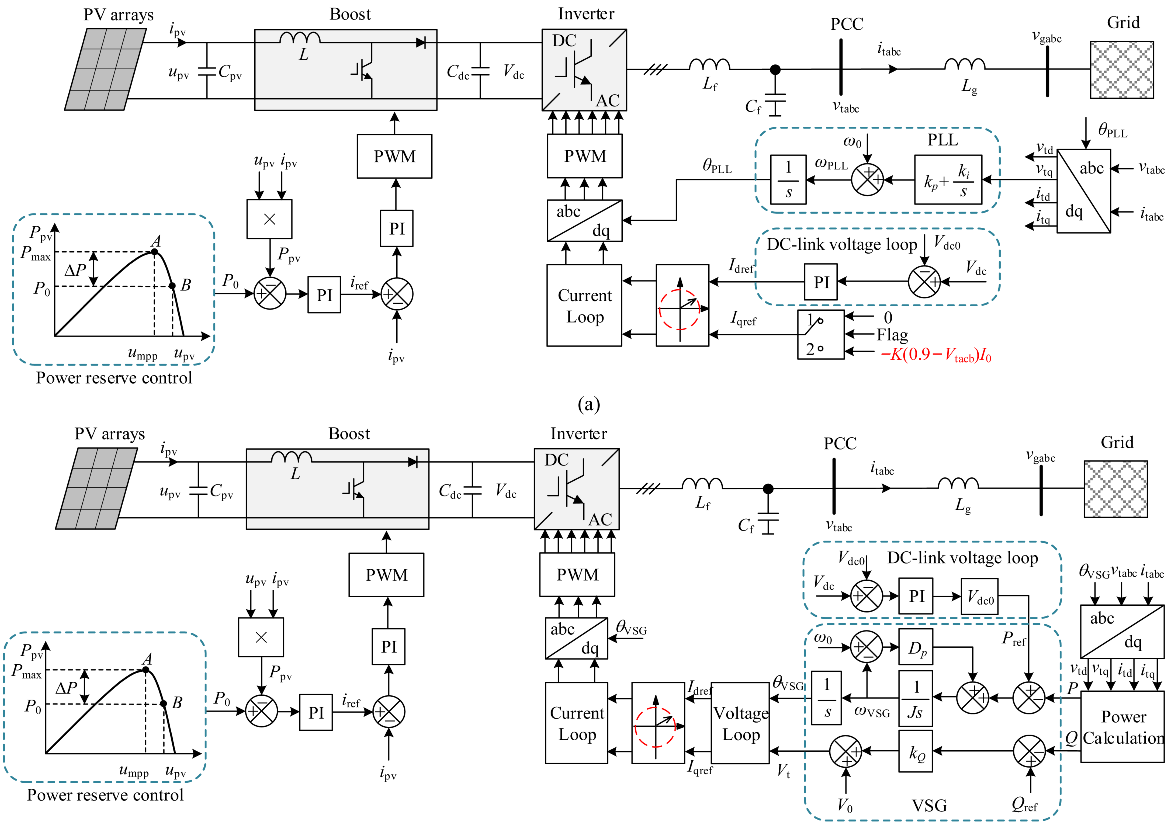

(a)

(b)

Fig. 1. System structure diagram of PV grid-tied system. (a) Grid-following control. (b) Grid-forming control.

TABLE I
SYSTEM MAIN PARAMETERS

Symbol	Description	Value
V_{dc0}	Rated dc-link voltage	1000 V
V_{g} (peak)	Grid voltage	311 V
ω_0	Rated frequency	100π rad/s
P_0	Rated power	10 kW
C_{dc}	Dc-link capacitor	10 mF
L_{g}	Grid inductance	15 mH
	Grid-following control	
k_{ppv} / k_{piv}	PI of dc-link voltage loop	2 / 80
k_p / k_i	PI of PLL	0.03 / 0.8
	Grid-forming control	
k_{pv} / k_{iv}	PI of dc-link voltage loop	0.03 / 0.1
J	Virtual inertia	20
D_p	Virtual damping coefficient	320
Q_{ref}	Reactive power reference	0
k_Q	Reactive power droop coefficient	0.01

Since the response of the inner current loop is faster than the PLL, it can ignore the dynamics of the inner current loop [30]. In the dq frame, the PCC voltage can be expressed as follows:

$$\begin{cases} V_{\mathrm{td}} = V_{\mathrm{g}}\cos(\theta_{\mathrm{g}} - \theta_{\mathrm{PLL}}) - I_{\mathrm{tq}}\omega_{\mathrm{PLL}}L_{\mathrm{g}} \\ V_{\mathrm{tq}} = V_{\mathrm{g}}\sin(\theta_{\mathrm{g}} - \theta_{\mathrm{PLL}}) + I_{\mathrm{td}}\omega_{\mathrm{PLL}}L_{\mathrm{g}}. \end{cases} \tag{2}$$

The angle difference between θ_{PLL} and θ_{g} is defined as δ_1. Based on the structure of the PLL, the expression of δ_1 is [17]

$$\delta_1 = \theta_{\mathrm{PLL}} - \theta_{\mathrm{g}} = \frac{1}{s}\left(k_p + \frac{k_i}{s}\right)(I_{\mathrm{td}}\omega_{\mathrm{PLL}}L_{\mathrm{g}} - V_{\mathrm{g}}\sin\delta_1) \tag{3}$$

where s is the differential operator.

As the current loop responds fast, it can be regarded that $I_{\mathrm{td}} = I_{\mathrm{dref}}$. However, I_{dref} is depended on the dc-link voltage loop. During the fault, the change of dc-link voltage brings the active current dynamics. Applying the differentiator on δ at both sides of (3) yields

$$\ddot{\delta}_1 = (k_p s + k_i)(I_{\mathrm{td}}\omega_{\mathrm{PLL}}L_{\mathrm{g}}) - (k_p s + k_i)(V_{\mathrm{g}}\sin\delta_1). \tag{4}$$

By considering the active current dynamics, the model of the GFL control can be built as

$$\begin{cases} \dot{\delta}_1 = \omega_{\mathrm{PLL}} - \omega_0 \\ \underbrace{(1 - k_p I_{\mathrm{td}} L_{\mathrm{g}})}_{J_{\mathrm{PLL}}}\ddot{\delta}_1 = \underbrace{\omega_0 L_{\mathrm{g}}(k_p s I_{\mathrm{td}} + k_i I_{\mathrm{td}})}_{P_{\mathrm{PLLref}}} - \underbrace{k_i V_{\mathrm{g}}\sin\delta_1}_{P_{\mathrm{PLLe}}} \\ \qquad - \underbrace{(k_p V_{\mathrm{g}}\cos\delta_1 - k_p L_{\mathrm{g}} s I_{\mathrm{td}} - k_i L_{\mathrm{g}} I_{\mathrm{td}})}_{D_{\mathrm{PLL}}}\dot{\delta}_1 \\ C_{\mathrm{dc}}V_{\mathrm{dc0}}\dot{V}_{\mathrm{dc}} = P_{\mathrm{in}} - P \\ I_{\mathrm{td}} = (V_{\mathrm{dc}} - V_{\mathrm{dc0}})(k_{ppv} + \frac{k_{piv}}{s}) \end{cases} \tag{5}$$

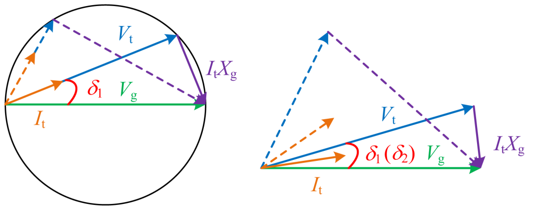

$I_{tq} = 0$ $I_{tq} \neq 0$

Fig. 2. Relationship between voltage and current.

where J_{PLL} is the equivalent inertia. D_{PLL} is the equivalent damping coefficient. P_{PLLref} is the equivalent mechanical power. P_{PLLe} is the equivalent electromagnetic power. P_{in} is the input active power provided by the PV source.

According to (5), when the active current dynamics are not considered, the dynamics of the PLL are the same as discussed in [17]. However, the dc-link voltage dynamics would change the active current and may misjudge the transient stability. J_{PLL}, P_{PLLref}, and D_{PLL} are all affected by the active current dynamics. The influence of the dc-link voltage dynamics can be analyzed with (5).

C. Grid-Forming Control

As shown in Fig. 1(b), to apply the VSG in the RES, the VSG is cascaded with the dc-link voltage loop, which gives the active power reference P_{ref} [8].

The angle difference between θ_{VSG} and θ_g is defined as δ_2. Considering the dc-link voltage loop and the VSG, the model of the GFM control can be established as

$$\begin{cases} \dot{\delta}_2 = \omega_{VSG} - \omega_0 \\ J\ddot{\delta}_2 = P_{ref} - P - D_p\dot{\delta}_2 \\ C_{dc}V_{dc0}\dot{V}_{dc} = P_{in} - P \\ P_{ref} = V_{dc0}(V_{dc} - V_{dc0})(k_{pv} + \frac{k_{iv}}{s}). \end{cases} \tag{6}$$

According to (6), the dc-link voltage dynamics only change the active power reference. The virtual inertia and the virtual damping are not affected and they can keep in the constants. The influence of the dc-link voltage dynamics can be analyzed with (6).

III. POWER TRANSMISSION AND TRANSIENT STABILITY ANALYSIS

A. Influence of Reactive Power

The reactive power impacts the active power. The relationship between the PCC voltage V_t, the grid impedance voltage I_tX_g, and the grid voltage V_g can be described as

$$\boldsymbol{V}_t + j\boldsymbol{I}_tX_g = \boldsymbol{V}_g \tag{7}$$

where $X_g = \omega_0 L_g$ is the grid reactance.

Fig. 2 shows the relationship among V_t, I_tX_g, and V_g. For the GFL control, both $I_{tq} = 0$ and $I_{tq} \neq 0$ would occur since the reactive current is given by I_{qref},. For the GFM control, I_{tq} is not zero because it needs the reactive power to support V_t. Obviously, when $I_{tq} = 0$, V_t, I_tX_g, and V_g can compose a right triangle, and the direction of V_t and I_tX_g are perpendicular to each other.

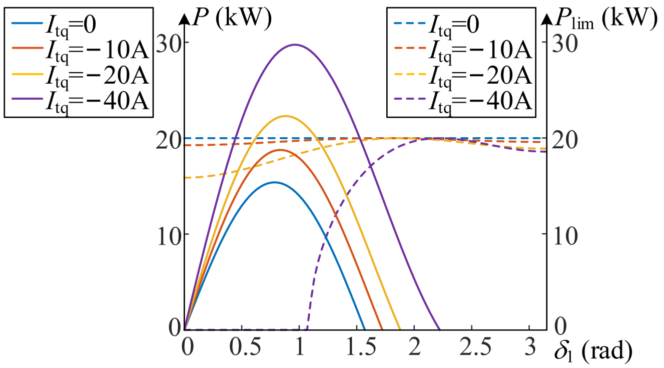

Fig. 3. Influence of reactive current on active power of GFL control.

When $I_{tq} = 0$, the relationship between the PCC voltage and the grid voltage can be expressed as

$$V_t = V_g \cos\delta_1. \tag{8}$$

According to the circuit of the Fig. 1(a), the active power transmission can be calculated as

$$P = \frac{3V_tV_g}{2X_g}\sin\delta_1 = \frac{3V_g^2}{4X_g}\sin(2\delta_1). \tag{9}$$

Obviously, the maximum active power transmission is $3{V_g}^2/(4X_g)$ when δ_1 is equal to $\pi/4$ instead of $\pi/2$. To maintain stability, δ_1 must smaller than $\pi/4$.

When $I_{tq} \neq 0$, V_t, I_tX_g, and V_g cannot compose a right triangle. In the steady state, the q-axis voltage of V_t is zero and $\omega_{PLL} = \omega_0$. According to (2), the PCC voltage is

$$V_t = V_{td} = V_g\cos\delta_1 - I_{tq}X_g. \tag{10}$$

To support the PCC voltage, the reactive current is negative. Based on (10), the active power transmission can be calculated as

$$P = \frac{3V_tV_g}{2X_g}\sin\delta_1 = \frac{3V_g^2}{4X_g}\sin(2\delta_1) - \frac{3V_gI_{tq}}{2}\sin\delta_1. \tag{11}$$

The reactive power transmission can be calculated as

$$Q = \frac{3(V_t^2 - V_tV_g\cos\delta_1)}{2X_g} = 1.5(I_{tq}^2X_g - V_gI_{tq}\cos\delta_1). \tag{12}$$

The active power transmission is limited due to the equipment capacity. The limited active power is

$$P_{lim} = \sqrt{S_{max}^2 - Q^2} \tag{13}$$

where S_{max} is the maximum capacity of the grid-tied inverter.

Based on (11)–(13), the curve of P and P_{lim} can be obtained, as displayed in Fig. 3. The solid line is the curve of P and the dotted line is the curve of P_{lim}. The maximum power transmission is small and its corresponding power angle is equal to $\pi/4$ when the reactive current is zero. The maximum power transmission and its corresponding power angle increase with the rising of reactive current. When δ_1 is small, V_t is much larger than V_g with the influence of the reactive current and the reactive power

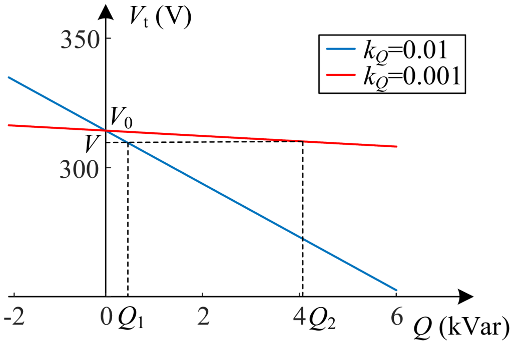

Fig. 4. Droop curve of reactive power and voltage.

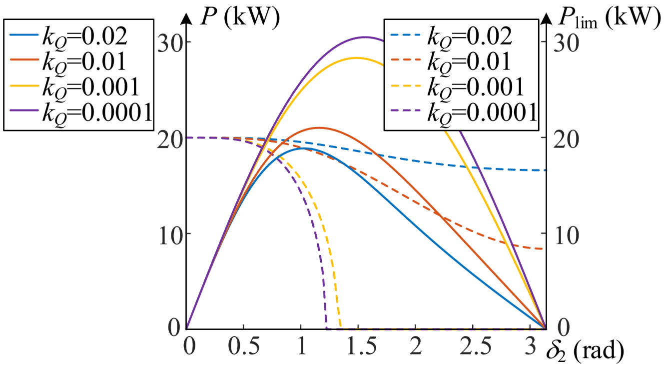

Fig. 5. Influence of k_Q on active power of GFM control.

is large. According to (12), the reactive power would reduce with the increasing of δ_1. Hence, P_{lim} is increased. Obviously, there is no intersection point between P and P_{lim} when $I_{\mathrm{tq}} > -10$ A. It means that the power transmission is limited by the grid inductance. However, there are intersection points between P and P_{lim} when $I_{\mathrm{tq}} < -20$ A. The power transmission is limited by the capacity of the GFL inverter. As displayed in Fig. 3, to output more active power, the reactive current is suitable in the range of -10 A to -20 A. In this way, the GFL inverter can output more active power and is not affected by its capacity.

Since the reactive current of the GFM inverter is not zero. V_{t}, $I_{\mathrm{t}}X_{\mathrm{g}}$, and V_{g} cannot compose a right triangle. Due to the reactive power control, its control law is

$$V_{\mathrm{t}} = V_0 + k_Q(Q_{\mathrm{ref}} - Q). \tag{14}$$

Based on (14), Fig. 4 depicts the Q-V droop characteristics with various k_Q. As can be seen, V_{t} is smoother with a smaller k_Q which needs more reactive power. It means that a smaller k_Q can support voltage better. However, the active power and the reactive power are coupled, the power transmission characteristic can be described as

$$\begin{cases} P = \frac{3V_{\mathrm{t}}V_{\mathrm{g}}}{2X_{\mathrm{g}}}\sin\delta_2 \\ Q = \frac{3(V_{\mathrm{t}}^2 - V_{\mathrm{t}}V_{\mathrm{g}}\cos\delta_2)}{2X_{\mathrm{g}}}. \end{cases} \tag{15}$$

Based on (14) and (15), the PCC voltage amplitude can be calculated as

$$V_{\mathrm{t}} = \sqrt{\left(\frac{X_{\mathrm{g}}}{3k_Q} - \frac{V_{\mathrm{g}}\cos\delta_2}{2}\right)^2 + \frac{2X_{\mathrm{g}}(V_0 + k_Q Q_{\mathrm{ref}})}{3k_Q}} - \left(\frac{X_{\mathrm{g}}}{3k_Q} - \frac{V_{\mathrm{g}}\cos\delta_2}{2}\right). \tag{16}$$

It can be seen that V_{t} is affected by Q_{ref} and k_Q. Hence, the active power is influenced by Q_{ref} and k_Q through V_{t}. Substituting (16) into (15), the active power transmission is

$$P = \frac{3V_{\mathrm{g}}}{2X_{\mathrm{g}}}\left[\sqrt{\left(\frac{X_{\mathrm{g}}}{3k_Q} - \frac{V_{\mathrm{g}}\cos\delta_2}{2}\right)^2 + \frac{2X_{\mathrm{g}}(V_0 + k_Q Q_{\mathrm{ref}})}{3k_Q}} - \left(\frac{X_{\mathrm{g}}}{3k_Q} - \frac{V_{\mathrm{g}}\cos\delta_2}{2}\right)\right]\sin\delta_2. \tag{17}$$

The active power transmission is limited due to the equipment capacity. Based on (15)–(17), the limited active power is

$$P_{\mathrm{lim}} = \sqrt{S_{\mathrm{max}}^2 - Q^2}. \tag{18}$$

Based on (17) and (18), the active power transmission characteristic can be obtained with various k_Q. As shown in Fig. 5, the solid line is the curve of P and the dotted line is the curve of P_{lim}. The maximum power transmission and its corresponding power angle decrease with the increasing of k_Q. According to (6) and (17), while k_Q is large, it may result in a small P and there is a risk of no equilibrium point. Hence, a large k_Q endangers the transient stability of the GFM inverter. A small k_Q is helpful to increase the maximum power transmission, but a small k_Q would result a large reactive power to support the PCC voltage and it is easy to trigger the current saturation. According to (16), when $\delta_2 = 0$, $V_{\mathrm{t}} = V_{\mathrm{g}}$ and the reactive power is 0. V_{t} becomes small and the reactive power becomes large with the increasing of δ_2, which results in the reduction of P_{lim}. As displayed in Fig. 5, to output more active power, k_Q is suitable in the range of 1/100 – 1/50. In this way, the GFM inverter can output more active power and is not affected by its capacity.

Compared with Figs. 3 and 5, it can be obtained that the GFL inverter is more prone to be constrained by its capacity and cannot output the active power. Since the reactive current of the GFL inverter is directly given, its initial voltage and reactive power are very large, and the active power of the GFL inverter is directly embedded, which results in the failure of the GFL inverter to output active power. The voltage of the GFM inverter is more stable, its initial reactive power is small. When δ_2 is small, the active power of the GFM inverter is not constrained by its capacity, and it can output active power even if k_Q is small.

B. Transient Stability Analysis of Grid-Following Control

Based on (11), the output active power would reduce as the gird voltage drops, which leads to the increment of the dc-link voltage. According to (5), when the output active power

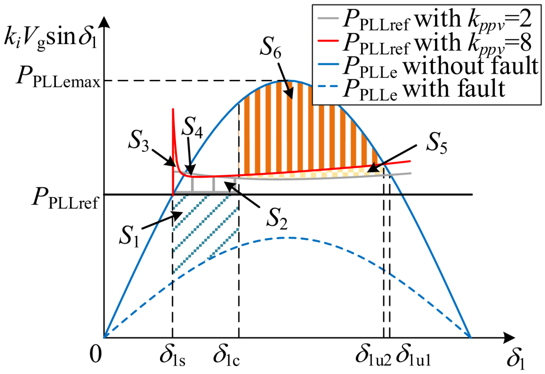

Fig. 6. Influence of k_{ppv} on equivalent power curve of GFL control when $V_{\rm g}$ drops from 1 to 0.48 p.u. Under the influence of the dc-link dynamics, $P_{\rm PLLref}$ cannot keep in a constant. $P_{\rm PLLref}$ becomes to the gray line with $k_{ppv} = 2$ and becomes to the red line with $k_{ppv} = 8$.

decreases, the active current would increase to

$$I_{\rm td} = \frac{P_{\rm in}-P}{C_{\rm dc}V_{\rm dc0}\,s}\left(k_{ppv}+\frac{k_{piv}}{s}\right). \tag{19}$$

When the active power of the GFL inverter decreases, it increases the change rate of the active current and the increment of the active current increase. According to (5), $P_{\rm PLLref}$ would increase and $D_{\rm PLL}$ would decrease. As the change rate of the active current increases fast and the active current increases a lot, the equivalent mechanical power would increase and the equivalent damping would be negative, which deteriorate the transient stability. To ensure the positive equivalent damping, δ_1 is supposed to lie within the range of $[\delta_{\rm min}, \delta_{\rm max}]$. $\delta_{\rm min}$ and $\delta_{\rm max}$ can be calculated by solving $D_{\rm PLL} = 0$.

According to (5), the equivalent power curve of the GFL inverter is obtained based on the numerical method. As shown in Fig. 6, under the influence of the dc-link voltage dynamics, $P_{\rm PLLref}$ cannot keep in a constant, it becomes to the gray line or the red line, the acceleration area increases and the maximum deceleration area decreases. The dc-link voltage responses fast when k_{ppv} increases and it results in the rapid increasing of the active current. When k_{ppv} is increased from 2 to 8, the acceleration area increases by $(S_3 - S_4)$ and the maximum deceleration area decreases by S_5. Reducing $C_{\rm dc}$ can also make the response of the dc-link voltage fast, which results in a larger acceleration area and a smaller maximum deceleration area. Therefore, increasing k_{ppv} and reducing $C_{\rm dc}$ endanger the transient stability.

When the grid voltage drops to 0.48 p.u., the phase portrait under different $C_{\rm dc}$ and k_{ppv} is shown in Fig. 7. When k_{ppv} is increased, the dc-link voltage responds fast and results in the increasing of $P_{\rm PLLref}$ and $\omega_{\rm PLL}$, and finally the GFL inverter loses stability. A small $C_{\rm dc}$ can also speed up the response of the dc-link voltage, and eventually results in the transient instability. As displayed in Fig. 7, $\delta_{\rm max}$ cannot exceed $\pi/2$, which is affected by $D_{\rm PLL}$. Therefore, the dc-link voltage dynamics are harmful to the transient stability of the GFL inverter. A fast response of the dc-link voltage would increase the risk of transient instability.

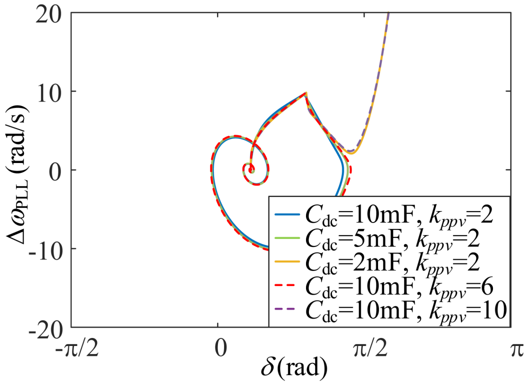

Fig. 7. Phase portrait of GFL control with various $C_{\rm dc}$ and k_{ppv}.

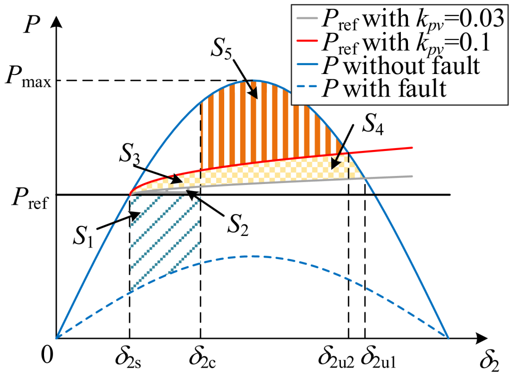

Fig. 8. Influence of k_{pv} on power curve of GFM control when $V_{\rm g}$ drops from 1 to 0.35 p.u. Under the influence of the dc-link dynamics, $P_{\rm ref}$ cannot keep in a constant. $P_{\rm ref}$ becomes to the gray line with $k_{pv} = 0.03$ and becomes to the red line with $k_{pv} = 0.1$.

C. Transient Stability Analysis of Grid-Forming Control

Based on (17), the output active power would reduce as the gird voltage drops, which leads to the increment of the dc-link voltage. When the active power decreases, the active power reference of the VSG would increase. According to (6), the active power reference can be described as

$$P_{\rm ref} = \frac{P_{\rm in}-P}{C_{\rm dc}\,s}\left(k_{pv}+\frac{k_{iv}}{s}\right). \tag{20}$$

Different from the GFL control, only $P_{\rm ref}$ is affected by the dc-link voltage dynamics, D_p can keep in a constant. When the active power decreases, the active power reference of the VSG would increase, and the increment of $P_{\rm ref}$ is related to the speed of the response of the dc-link voltage.

According to (6), the power curve of the GFM inverter is shown in Fig. 8 based on the numerical method. Under the influence of the dc-link voltage dynamics, $P_{\rm ref}$ becomes to the gray line or the red line, the acceleration area increases and the maximum deceleration area decreases. When k_{pv} is increased from 0.03 to 0.1, the dc-link voltage responses become faster. The acceleration area increases from $(S_1 + S_2)$ to $(S_1 + S_2 + S_3)$ and the maximum deceleration area decreases from $(S_4 + S_5)$ to S_5. Since the response of the dc-link voltage is fast with a

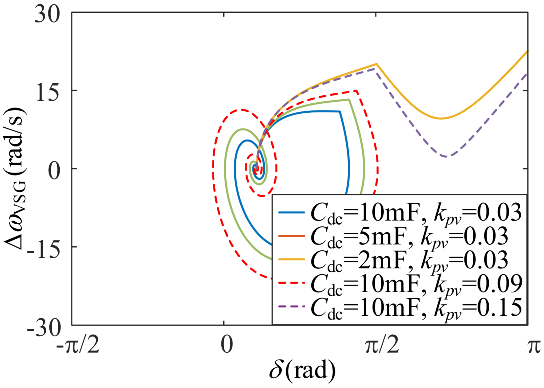

Fig. 9. Phase portrait of GFM control with various C_{dc} and k_{pv}.

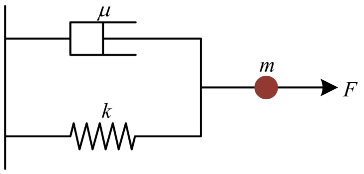

Fig. 10. Mass-spring-damper system.

small C_{dc} and it leads to a larger acceleration area and a smaller maximum deceleration area. Hence, increasing k_{pv} and reducing C_{dc} endanger the transient stability.

When the grid voltage drops to 0.35 p.u., the phase portrait with various C_{dc} and k_{pv} is shown in Fig. 9. With the increasing of k_{pv}, the dc-link voltage responds fast, which introduces the increasing of P_{ref}. Based on (6), ω_{VSG} would increase as P_{ref} rises. When the dc-link voltage responds fast, the acceleration area increases and ω_{VSG} can move further and eventually result in the transient instability. It shows that the dc-link voltage dynamics are harmful to the transient stability of the GFM inverter. It is the same as the GFL inverter, a fast response of the dc-link voltage increases the risk of transient instability. Different from the GFL inverter, δ_2 can still recover the stability while it exceeds $\pi/2$ since D_p is always positive. Thus, the GFM inverter can maintain the stability with a more severe grid voltage drop.

IV. ENHANCEMENT FOR TRANSIENT STABILITY

A. Basic Principle

The mass-spring-damper system is constituted of a spring and a damper, as shown in Fig. 10. The spring and the damper are parallel. The mass point moves under the elastic force, the damping force and the forcing force. When the mass point is subjected to an external force, the spring would provide a force which the direction is always opposite to the external force. The damper can be regarded as a piston hydraulic cylinder system. When the relative movement exists between the piston and the hydraulic cylinder, the active side is always subjected to the damping force of the other side. For the linear damper, the magnitude of the damping force is proportional to the relative speed of the movement of the damper. The kinetic equation of the mass point satisfies

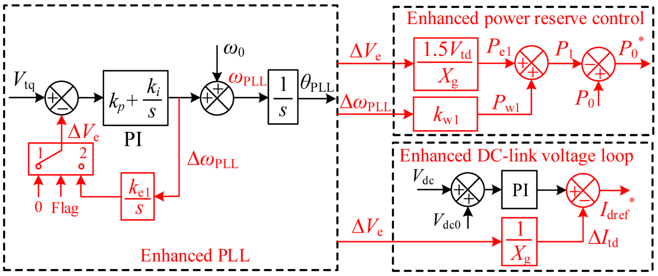

Fig. 11. Enhancement for GFL control.

$$\begin{cases}\dot{x}=v\\ m\ddot{x}=F-kx-\mu\dot{x}\end{cases}\tag{21}$$

where m is the mass of the mass point, k is the elastic coefficient of the spring, μ represents the damping coefficient of the damper, F denotes the forcing force, x is the displacement of the mass point relative to its initial position, and v is the velocity of the mass point.

The mass point is stable in the initial position when F is zero. However, the mass point would leave the initial position once F is not equal to zero. When the spring produces the elastic force equal to the forcing force, the mass-spring-damper system can keep stable. The system can always restore the stability under the elastic force.

B. Enhancement for Grid-Following Control

Based on (5), ($P_{\mathrm{PLLref}}-P_{\mathrm{PLLe}}$) can be regarded as the equivalent forcing force. Obviously, there is no equivalent elastic force. To introduce the equivalent elastic force for the GFL control, $\Delta\omega_{\mathrm{PLL}}$ is fed back and then goes through the integrator, as shown in Fig. 11. Based on the structure of Fig. 11, the characteristic of the enhanced PLL can be described as

$$\begin{cases}\dot{\delta}_1=\omega_{\mathrm{PLL}}-\omega_0\\ \underbrace{(1-k_pI_{\mathrm{td}}L_{\mathrm{g}})}_{J_{\mathrm{PLL}}}\ddot{\delta}_1=\underbrace{\omega_0L_{\mathrm{g}}(k_psI_{\mathrm{td}}+k_iI_{\mathrm{td}})}_{P_{\mathrm{PLLref}}}-\underbrace{k_iV_{\mathrm{g}}\sin\delta_1}_{P_{\mathrm{PLLe}}}-\underbrace{k_ik_{\mathrm{e1}}\delta_1}_{P_{\mathrm{e}}}\\ \qquad-\underbrace{(k_pV_{\mathrm{g}}\cos\delta_1+k_pk_{\mathrm{e1}}-k_pL_{\mathrm{g}}sI_{\mathrm{td}}-k_iL_{\mathrm{g}}I_{\mathrm{td}})}_{D_{\mathrm{PLL}}}\dot{\delta}_1\end{cases}\tag{22}$$

where P_{e} is the equivalent elastic force.

It should note that the equivalent elastic force introduces the steady-state error. Hence, the equivalent elastic force is removed when the GFL inverter operates in the normal condition. The enhanced GFL control is the same as the traditional GFL control at Flag $=1$. The equivalent elastic force is introduced at Flag $=2$. The value of Flag is determined by V_{t}, and the voltage threshold V_{th} is set to 0.9 p.u. according to the grid code. When $V_{\mathrm{t}}>V_{\mathrm{th}}$, Flag is set to 1. When $V_{\mathrm{t}}\leq V_{\mathrm{th}}$, Flag is set to 2.

Since the active current reference is given by the dc-link voltage loop, even if the equivalent elastic force is added into the PLL, the active power would be unbalanced at the input

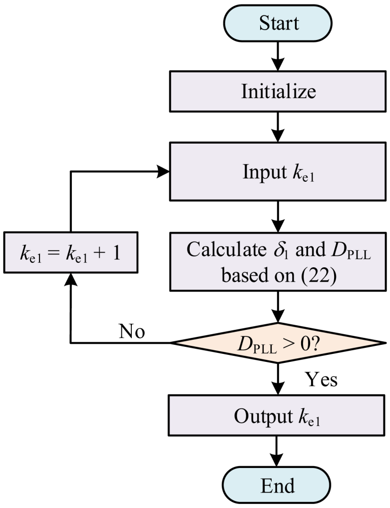

Fig. 12. Design process of k_{e1}.

and output of the dc-link capacitor. The active current reference would increase when active power decreases. Consequently, the equivalent elastic power P_{e1} is added into the power reserve control to regulate the active power of the PV source, as shown in Fig. 11.

When the GFL control operates steadily, the input of the enhanced PLL is

$$\left(I_{\mathrm{td}} - \frac{k_{\mathrm{e1}}\delta_1}{X_{\mathrm{g}}}\right) X_{\mathrm{g}} - V_{\mathrm{g}} \sin\delta_1 = 0. \tag{23}$$

Compared with the traditional PLL, the active current should be corrected as

$$I^*_{\mathrm{dref}} = I_{\mathrm{td}} - \frac{k_{\mathrm{e1}}\delta_1}{X_{\mathrm{g}}}. \tag{24}$$

Hence, the equivalent elastic current is as

$$\Delta I_{\mathrm{td}} = \frac{k_{\mathrm{e1}}\delta_1}{X_{\mathrm{g}}}. \tag{25}$$

The equivalent elastic power caused by the equivalent elastic current is

$$P_{\mathrm{e1}} = 1.5 V_{\mathrm{td}} \Delta I_{\mathrm{td}} = \frac{1.5 V_{\mathrm{td}} k_{\mathrm{e1}} \delta_1}{X_{\mathrm{g}}}. \tag{26}$$

Based on (26), the equivalent elastic power is large and it causes the small output active power of the PV source when k_{e1} is large. To output more active power, a suitable k_{e1} should be designed. Based on (22), k_{e1} can be designed as follows:

$$\begin{cases} \omega_0 L_{\mathrm{g}}(k_p s I_{\mathrm{td}} + k_i I_{\mathrm{td}}) - k_i V_{\mathrm{g}} \sin\delta_1 - k_i k_{\mathrm{e1}}\delta_1 = 0 \\ D_{\mathrm{PLL}} = k_p V_{\mathrm{g}} \cos\delta_1 + k_p k_{\mathrm{e1}} - k_p L_{\mathrm{g}} s I_{\mathrm{td}} - k_i L_{\mathrm{g}} I_{\mathrm{td}} > 0 \end{cases} \tag{27}$$

δ_1 is changed with various k_{e1} and the equivalent damping would be negative when k_{e1} is small and δ_1 is large. It should redesign k_{e1} to ensure the active power balance and the positive equivalent damping. Hence, the appropriate k_{e1} is designed by iterative calculation. The design process is shown in Fig. 12. First, inputting k_{e1} and calculating δ_1 and k_{e1} based on (22). Then, determining whether D_{PLL} is positive. If D_{PLL} is negative, k_{e1} should be increased and recalculating D_{PLL}. If D_{PLL} is positive, k_{e1} is designed and can be output.

To support the grid frequency, the frequency deviation feedback is introduced into the power reserve control. When the grid frequency falls, the output active power of the PV source increases by P_{w1}

$$P_{\mathrm{w1}} = k_{\mathrm{w1}} \Delta\omega_{\mathrm{PLL}}. \tag{28}$$

The PV source should continuously operate when the frequency is in the range of 48.5 to 50.5 Hz. And the increment amplitude of the active power ΔP_{t} should satisfy the Chinese standard [29]

$$\Delta P_{\mathrm{t}} = K_{\mathrm{f}} \frac{\Delta\omega}{\omega_0} P_0 \tag{29}$$

where K_{f} is the active power frequency control coefficient and it is in the range of 10 to 50.

To satisfy the rule, $P_{\mathrm{w1}} = \Delta P_{\mathrm{t}}$. Thus, k_{w1} is designed based on (28) and (29)

$$k_{\mathrm{w1}} = \frac{K_{\mathrm{f}} P_0}{\omega_0}. \tag{30}$$

Based on the standard of [29], the reserved power can be designed as

$$\Delta P = \Delta P_{\mathrm{t}} = K_{\mathrm{f}} \frac{\Delta\omega}{\omega_0} P_0. \tag{31}$$

According to (1) and (28), the power reserved factor is designed as

$$\alpha = \frac{K_{\mathrm{f}}\Delta\omega}{K_{\mathrm{f}}\Delta\omega + \omega_0}. \tag{32}$$

The grid short circuit ratio (SCR) is defined as [31]

$$\mathrm{SCR} = \frac{S}{P_0} = \frac{3V_{\mathrm{g}}^2}{2P_0 X_{\mathrm{g}}} \tag{33}$$

where S is the short-circuit capacity and P_0 is the active power injection of the RESs.

For the GFL control, when the inverter normally operates, I_{tq} is zero. The rated active power is equal to the steady-state value of active power. According to (9), the rated active power can be calculated as

$$P_0 = \frac{3V_{\mathrm{g}}^2}{4X_{\mathrm{g}}} \sin(2\delta_{10}) \le \frac{3V_{\mathrm{g}}^2}{4X_{\mathrm{g}}}. \tag{34}$$

Based on (33) and (34), the grid SCR_1 of the GFL control should satisfy

$$\mathrm{SCR}_1 = \frac{3V_{\mathrm{g}}^2}{2P_0 X_{\mathrm{g}}} \ge 2. \tag{35}$$

C. Enhancement for Grid-Forming Control

Based on (6), $(P_{\mathrm{ref}} - P)$ can be regarded as the equivalent forcing force. Compared to the mass-spring-damper system, the GFM control lacks the elastic force. When the grid voltage drops severely, $(P_{\mathrm{ref}} - P)$ may be not equal to zero and causes the insufficient deceleration area. δ_2 would increase and cannot keep

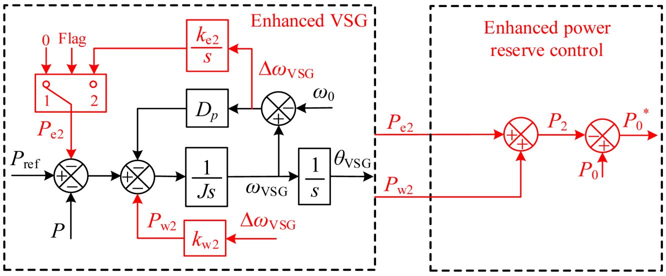

Fig. 13. Enhancement for GFM control.

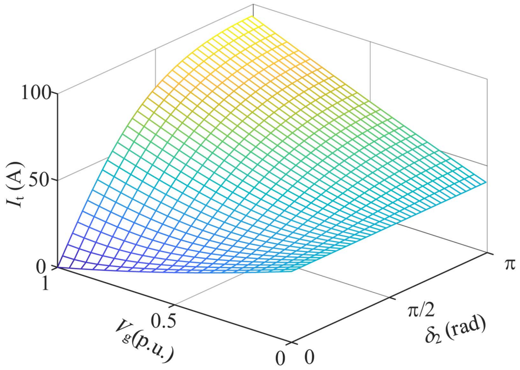

Fig. 14. Current amplitude with different grid voltage dip.

stable. Finally, the GFM inverter loses stability. To enhance the transient stability, the equivalent elastic force is introduced in the VSG. $\Delta\omega_{\mathrm{VSG}}$ is fed back and then goes through the integrator, as shown in Fig. 13. To support the grid frequency, the frequency deviation feedback is introduced into the power reserve control. When the grid frequency falls, the output active power of the PV source increases by P_{w2}. Based on the structure of Fig. 13, the characteristic of the enhanced VSG can be described as

$$\begin{cases} \dot{\delta}_2 = \omega_{\mathrm{VSG}} - \omega_0 \\ J\ddot{\delta}_2 = P_{\mathrm{ref}} - P - \underbrace{k_{\mathrm{e2}}\delta_2}_{P_{\mathrm{e2}}} - \underbrace{k_{\mathrm{w2}}\dot{\delta}_2}_{P_{\mathrm{w2}}} - D_p\dot{\delta}_2 \end{cases} \tag{36}$$

where P_{e2} is the equivalent elastic force.

It is the same as the enhanced GFL control, the equivalent elastic force introduces the steady-state error. Hence, the equivalent elastic force is introduced at Flag = 2. The enhanced GFM control is the same as the traditional GFM control at Flag = 1. When $V_{\mathrm{t}} > V_{\mathrm{th}}$, Flag is set to 1. When $V_{\mathrm{t}} \leq V_{\mathrm{th}}$, Flag is set to 2.

Since the active power reference is provided by the dc-link voltage loop, even if P_{e2} and P_{w2} are added into the VSG, the active power would be unbalanced at the input and output of the dc-link capacitor. And P_{ref} would increase when the grid active power decreases. To avoid the increasing of P_{ref}, P_{e2}, and P_{w2} are added into the power reserve control to regulate the output active power of the PV source, as shown in Fig. 13. Based on (36), the frequency deviation feedback can increase the virtual damping of the VSG. To support the grid frequency, k_{w2} can be designed based on [29].

The transient stability can be enhanced and the active power can output as much as possible by designing a suitable k_{e2}. Although a large k_{e2} is beneficial to the transient stability, it makes the small δ_2 and decreases the output active power. To output more active power, k_{e2} cannot be designed too large. However, when k_{e2} is small, there is still a risk of insufficient deceleration area and it may trigger the current saturation. To avoid triggering the current saturation and output more active power, it is necessary to consider the change of the current under different δ_2. The current amplitude can be calculated as

$$I_{\mathrm{t}} = \frac{|V_{\mathrm{t}}\angle\delta_2 - V_{\mathrm{g}}|}{X_{\mathrm{g}}}. \tag{37}$$

According to (16) and (37), it obtains the current amplitude with different grid voltage drops, as shown in Fig. 14. When the grid voltage drop is large, the current has a slight change with various δ_2. When the grid voltage drop is small, the current changes significantly with various δ_2. To avoid triggering the current saturation, k_{e2} is designed at the operating point, which easily exceeds the current saturation. When V_{t} is lower than 0.9 p.u., the equivalent elastic force added into the VSG. The maximum δ_2 is designed as $\delta_{2\mathrm{s}}$ which is the power angle when the current saturation is triggered. k_{e2} can be obtained as

$$k_{\mathrm{e2}} = \frac{P_0 - P|_{\delta_2 = \delta_{2\mathrm{s}}}}{\delta_{2\mathrm{s}}}. \tag{38}$$

According to (16), k_Q affects the active power of the VSG, it is necessary to consider the influence of k_Q and recalculate k_{e2}. Based on this, the appropriate k_Q and k_{e2} are designed by iterative calculation. The design process is shown in Fig. 15. First, based on (16) and (37), calculating the current with various grid voltage drops and determining whether I_{t} is smaller than the current saturation value $I_{\max}$. Then, determining whether $\delta_{2\mathrm{s}}$ is smaller than before. If $\delta_{2\mathrm{s}}$ is smaller than before, increasing k_Q and recalculating $\delta_{2\mathrm{s}.}$ If $\delta_{2\mathrm{s}}$ starts increasing, calculating k_{e2}. Finally, outputting k_Q and k_{e2}.

According to Fig. 5, the active power transmission is affected by k_Q. The rated active power is equal to the steady-state value of active power. Based (15), the relationship between the rated active power and the maximum active power is

$$P_0 = \frac{3V_{\mathrm{t}}V_{\mathrm{g}}}{2X_{\mathrm{g}}}\sin\delta_{20} \leq P_{\max}. \tag{39}$$

Based on (33) and (39), the grid SCR_2 of the GFM control should satisfy

$$\mathrm{SCR}_2 = \frac{3V_{\mathrm{g}}^2}{2P_0X_{\mathrm{g}}} \geq \frac{3V_{\mathrm{g}}^2}{2P_{\max}X_{\mathrm{g}}}. \tag{40}$$

V. VERIFICATION

The simulation and experiment are implemented to verify the theoretical analysis and the enhanced control.

A. Simulation Results of Grid-Following Control

The simulation results are conducted based on MATLAB/Simulink. The parameters of the system are given as Table I.

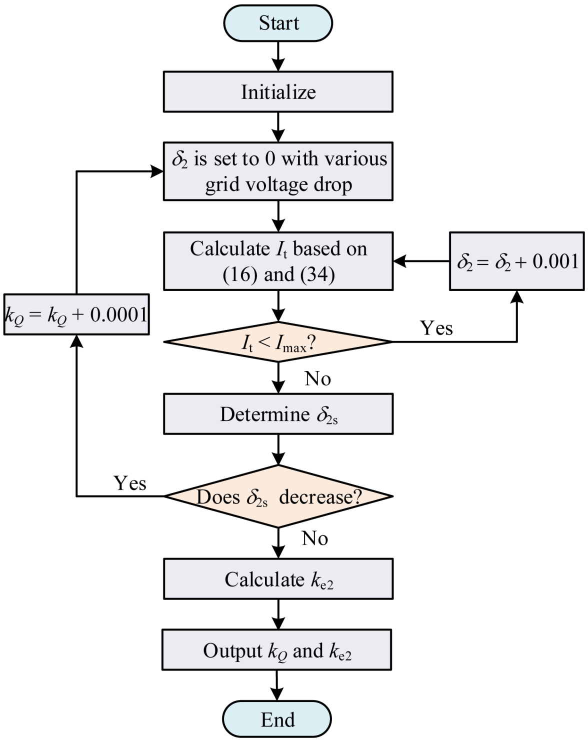

Fig. 15. Design process of k_Q and k_{e2}.

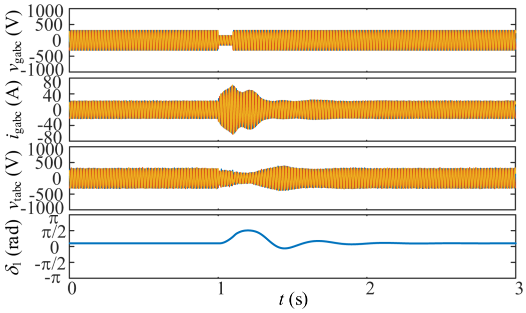

Fig. 16. Results of GFL inverter with grid voltage drop.

The grid voltage drops to 0.48 p.u. and its duration is 0.1 s. Fig. 16 shows the results of the GFL inverter. Under the grid voltage drop, the GFL inverter can recover the stability and it takes around 1 s to recover stability and its grid current THD is 1.37%. It meets the requirement in [32].

The same grid voltage drop is carried out while k_{ppv} is increased and C_{dc} is decreased. Compared to $k_{ppv} = 2$, the response of the dc-link voltage becomes faster with $k_{ppv} = 10$. It results in a larger acceleration area and a smaller maximum deceleration area. Compared to Fig. 16, a large k_{ppv} leads to the transient instability of the GFL inverter, as shown in Fig. 17. A small C_{dc} can also make a fast response of the dc-link voltage. Fig. 18 shows the results of the GFL inverter with $C_{\mathrm{dc}} = 2$ mF. Obviously, the GFL inverter loses stability with a small C_{dc}. Figs. 17 and 18 verify the transient stability analysis of a fast response of the dc-link voltage.

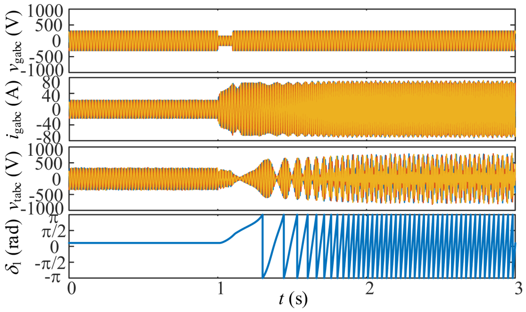

Fig. 17. Results of GFL inverter with k_{ppv} increased.

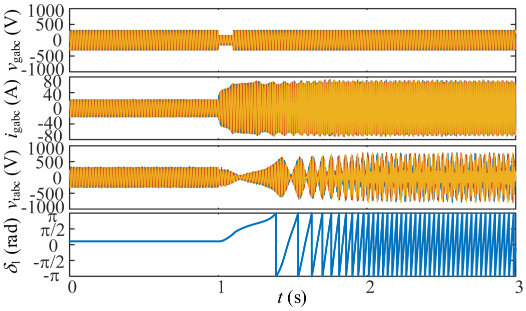

Fig. 18. Results of GFL inverter with C_{dc} decreased.

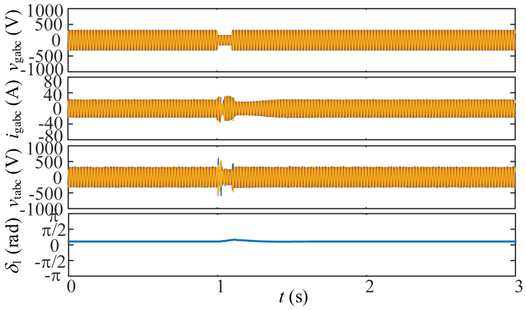

Fig. 19. Results of GFL inverter with enhanced control.

Fig. 19 displays the results of the GFL inverter with the enhanced control. k_{e1} is designed as 610 and k_{w1} is designed as 636. The grid voltage drops to 0.48 p.u. and its duration is 0.1 s. C_{dc} is set to 2 mF. Fig. 19 shows that the overshoot of grid current is 18%, the THD of the grid current is 1.37% and the GFL inverter with the enhanced control can recover stability within 0.4 s. The frequency deviation feedback and equivalent elasticity cooperative control can regulate the active power of the PV source, it improves the transient stability of the GFL inverter. It proves the effectiveness of the enhanced control.

To show the benefits of the enhanced control in this article, it compares with the control in [22]. The existing proposed control method diagram is shown in Fig. 20. This control can enhance the damping, but it still loses stability when the grid voltage drop is severe. When the grid voltage drops to 0.1 p.u., the proposed control in [22] triggers the current saturation and cannot keep stable, as shown in Fig. 21. The THD of the grid current is 1689%

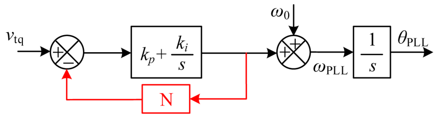

Fig. 20. Existing proposed control in [22].

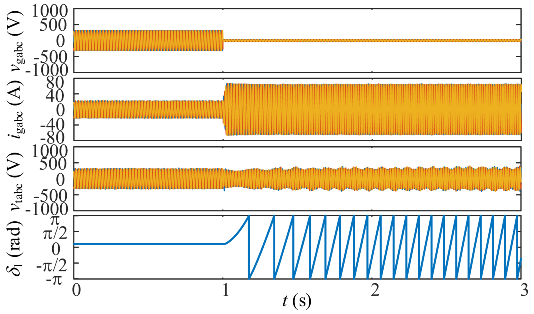

Fig. 21. Results of GFL inverter with active damping-based control [22].

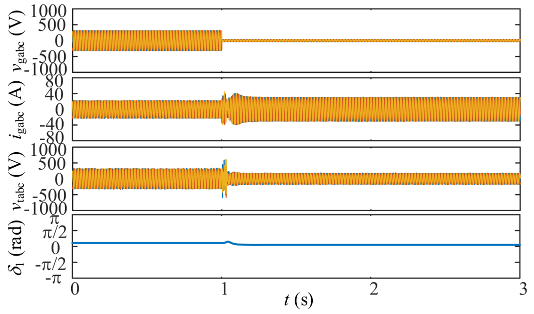

Fig. 22. Results of GFL inverter with enhanced control.

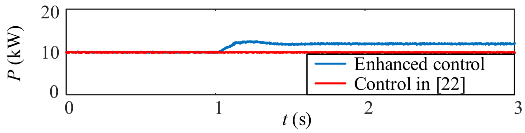

Fig. 23. Responses of GFL inverter with grid frequency fall.

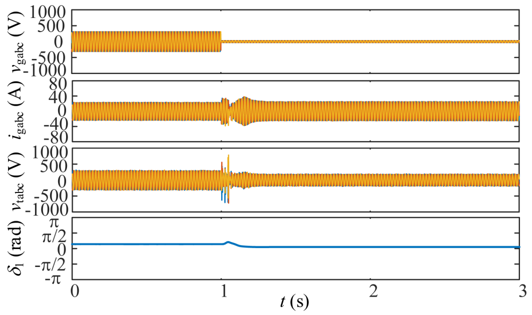

Fig. 24. Results of GFL control when SCR_1 is 2.3 with grid voltage drops.

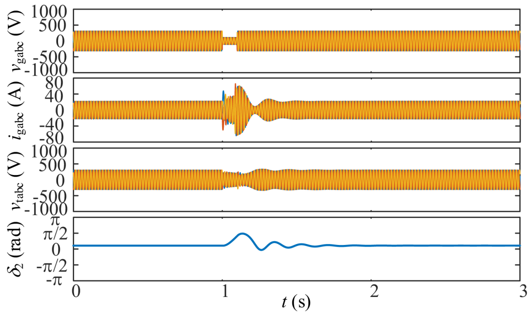

Fig. 25. Results of GFM inverter with grid voltage drop.

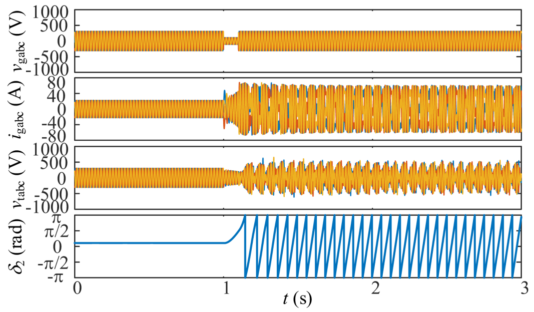

Fig. 26. Results of GFM inverter with k_{pv} increased.

after the fault, which does not meet the standard. After applying the enhanced control, the overshoot of grid current is 26%, the THD of the grid current is 1.37%, and the system can return to stability within 0.15 s, as shown in Fig. 22. To perform the grid frequency support capability, the grid frequency falls to 49.5 Hz at 1 s, the active power response is shown in Fig. 23. Obviously, the active power of the enhanced control in this article increases by 2 kW to support the grid frequency and its overshoot is 6.5%. It takes 0.3 s to recover stability. The proposed control in [22] cannot output more active power. The power reserve control with the enhanced control in this article is more stable and can support the grid frequency. The enhanced control performs well in the weak grid. The grid SCR_1 is 3 in Fig. 22 and the grid SCR_1 is 2.3 in Fig. 24. When the grid voltage drops to 0.1 p.u., the overshoot of grid current is 48%, the THD of grid current is 1.30% and the system can also restore stability after 0.24 s, as depicted in Fig. 24. The GFL control with the enhanced control can operate in the small grid SCR_1 and it can still restore stable under the severe grid fault.

B. Simulation Results of Grid-Forming Control

The grid voltage drops to 0.35 p.u. and its duration is 0.1 s. Fig. 25 shows the results of the GFM inverter. The GFM inverter can recover the transient stability with the grid voltage drop. It takes around 0.8 s to recover stability and its grid current THD is 0.28%.

To verify the influence of the dc-link voltage dynamics, the grid voltage drops to 0.35 p.u. and lasts for 0.1 s. Fig. 26 displays the results of the GFM inverter with $k_{pv} = 0.1$. With a larger k_{pv}, the GFM inverter has a larger acceleration area and a smaller maximum deceleration area. Under the grid voltage drop, the GFM inverter loses stability. Fig. 27 shows the results of the

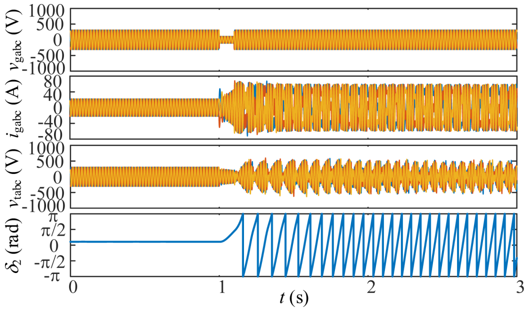

Fig. 27. Results of GFM inverter with C_{dc} decreased.

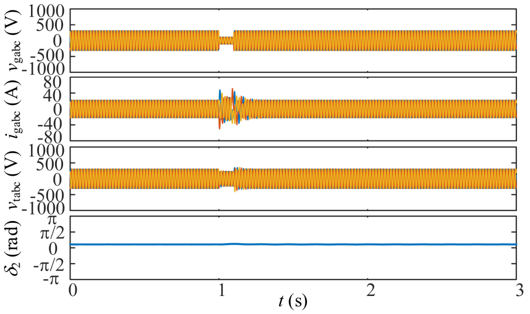

Fig. 28. Results of GFM inverter with enhanced control.

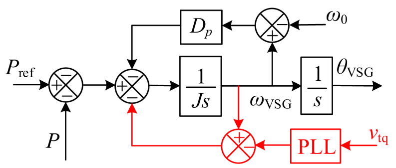

Fig. 29. Existing proposed control in [25].

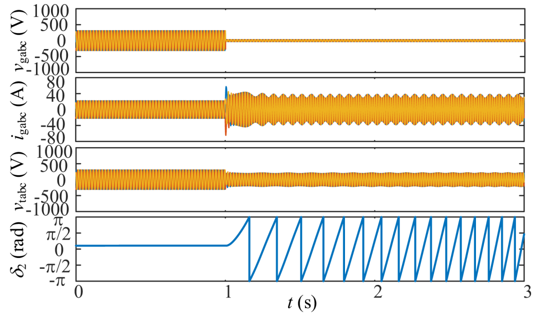

Fig. 30. Results of GFM inverter with active damping-based control [25].

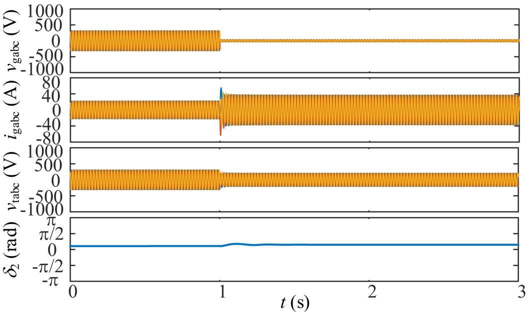

Fig. 31. Results of GFM inverter with enhanced control.

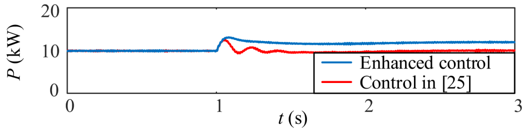

Fig. 32. Responses of GFM inverter with grid frequency fall.

GFM inverter with $C_{\mathrm{dc}} = 2$ mF, which cannot restore stability. Compared with Fig. 25, a small C_{dc} is harmful to the transient stability since the smaller C_{dc} causes a larger acceleration area and a smaller maximum deceleration area. Figs. 26 and 27 verify the influence of k_{pv} and C_{dc}.

Fig. 28 depicts the results of the GFM inverter with the enhanced control. k_{w2} is designed as 636. k_{e2} is designed as 19 330 and k_Q is designed as 0.0102 through the iterative calculation. The grid voltage drops to 0.35 p.u. and lasts for 0.1 s. C_{dc} is set to 2 mF. Although the overshoot of grid current is 40%, the THD of the grid current is 0.28% and the GFM inverter can recover stability within 0.25 s, as shown in Fig. 28. The frequency deviation feedback and equivalent elasticity cooperative control can improve the transient stability of the GFM inverter. It proves the effectiveness of the enhanced control.

To show the benefits of the enhanced control in this article, it compares with the proposed control in [25]. The existing control method diagram is shown in Fig. 29. This control only enhances the damping, it cannot regulate the active power of the PV source. It loses stability when the grid voltage drop is severe. The grid voltage drops to 0.1 p.u., the proposed control in [25] cannot keep stable, as shown in Fig. 30. The THD of the grid current is 631% after the fault, which does not meet the standard. The enhanced control in this article can keep stable, as shown in Fig. 31. The THD of the grid current is 0.28%, which still meets the standard. The overshoot of grid current is 38% and the system can restore stable after 0.1 s. At the same time, the enhanced control in this article can support the grid frequency. When grid frequency falls to 49.5 Hz at 1 s, the active power response is shown in Fig. 32. Obviously, the active power of the enhanced control in this article increases by 2 kW to support the grid frequency, and the overshoot is 8.8%. It takes 0.3 s to recover stability. The proposed control in [25] outputs less active power. Its overshoot is 24% and it recovers stability after 0.5 s. The power reserve control with the enhanced control in this article is more stable and can support the grid frequency. The enhanced control performs well in the weak grid. The grid SCR_2 is 3 in Fig. 31 and the grid SCR_2 is 1.6 in Fig. 33. When the grid voltage drops to 0.1 p.u., the overshoot of grid current is 58%, the THD of grid current is 0.16% and it takes 0.18 s to restore stable, as shown in Fig. 33. The GFM control with the enhanced control still performs well in the small grid SCR_2.

Fig. 34 shows the results of GFM control with various k_Q. The grid voltage drops to 0.1 p.u., and the GFM control would

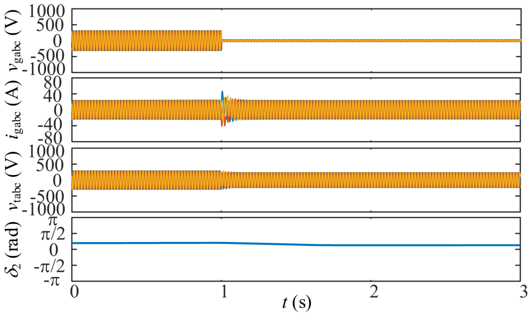

Fig. 33. Results of GFM control when SCR_2 is 1.6 with grid voltage drops.

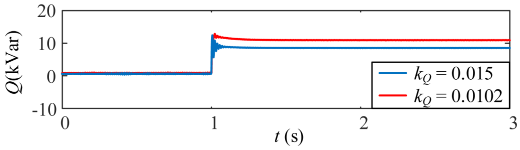

Fig. 34. Results with various k_Q with grid voltage drops to 0.1 p.u.

TABLE II
COMPARISONS OF EXISTING CONTROLS

Methods	Transient stability	Applicable fault types	Frequency support
Damping control for GFL inverter [22]	Stable with equilibrium point	Voltage drop	No
Enhanced control for GFL inverter	Stable	Voltage drop, frequency fault	Strong
Damping control for GFM inverter [25]	Stable with equilibrium point	Voltage drop	Slight
Enhanced control for GFM inverter	Stable	Voltage drop, frequency fault	Strong

output the reactive power to support the grid voltage. As shown in Fig. 34, the reactive power is increased to 8.7 kVar when k_Q is 0.015. When k_Q is reduced to 0.0102, the reactive power is increased to 11 kVar. It means that decreasing k_Q need to provide more reactive power to support voltage, but it increases the risk of triggering the current saturation for GFM control.

Based on the above results, the comparisons of the enhanced control in this article against the existing control are listed in Table II. The other damping control for the GFL or GFM inverter can only keep stable when the equilibrium point exists, and there is no grid frequency support capability or the grid frequency support capability is slight. The enhanced control for the GFL and GFM inverter in this article can keep stable under grid voltage drop and can support grid frequency. It greatly improves the fault ride-through capability and grid support capability of the inverter.

C. Power Hardware-in-Loop Experimental Results

Fig. 35 depicts the power hardware-in-loop experimental platform for the PV grid-tied system. The programmable dc source (Chroma 62100H-600S) has the PV array simulation function and it is used as the PV simulator. The PV simulator is connected to the Boost and the Boost is connected to the inverter. The inverter includes IGBT module, *LC* filter, and dc capacitor. The inverter is connected to the grid simulator through the grid inductance. The grid simulator is composed of the RTLAB (OP5707) and bidirectional power amplifier (EGSTON CSU200–1GAMP6-HV). The RTLAB is used to set the grid voltage. The bidirectional power amplifier is controlled as an ac voltage source by the RTLAB. The parameters of the system are given as Table III. The rated power is set to 1500 W due to the limitation of the equipment capacity.

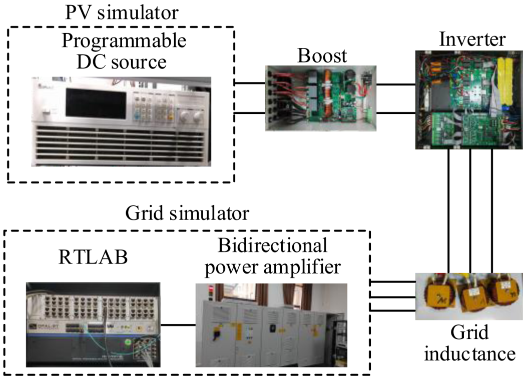

Fig. 35. Power hardware-in-loop platform.

TABLE III
EXPERIMENTAL PARAMETERS

Symbol	Description	Value
V_{dc0}	Rated dc-link voltage	250 V
V_g (peak)	Grid voltage	110 V
ω_0	Rated frequency	100π rad/s
P_0	Rated power	1500 W
C_{dc}	Dc-link capacitor	1645 uF
L_g	Grid inductance	4.5 mH
	Grid-following control	
k_{ppv} / k_{piv}	PI of dc-link voltage loop	0.1 / 2
k_p / k_i	PI of PLL	0.03 / 0.8
	Grid-forming control	
k_{pv} / k_{iv}	PI of dc-link voltage loop	0.005 / 0.05
J	Virtual inertia	2
D_p	Virtual damping coefficient	32
Q_{ref}	Reactive power reference	0
k_Q	Reactive power droop coefficient	0.08

When the programmable dc source is configured to emulate PV array, the voltage-current operating points must be predefined to generate the *P-V* characteristic curve. These parameters are preloaded into the dc source via the software Chroma Solar Array Simulation Soft Panel. The experimental *P-V* and *I-V* characteristics of the PV array are illustrated in Fig. 36. The voltage V_{mpp} is 207 V and the current I_{mpp} is 11.1 A in the maximum power point.

The experimental results of the GFL inverter are shown in Figs. 37–39. The grid current THD is 3.18%. When the grid voltage drops to 0.2 p.u., the GFL inverter triggers the current saturation and loses stability, as shown in Fig. 37. Since triggering the protection, the inverter is blocked. After applying the

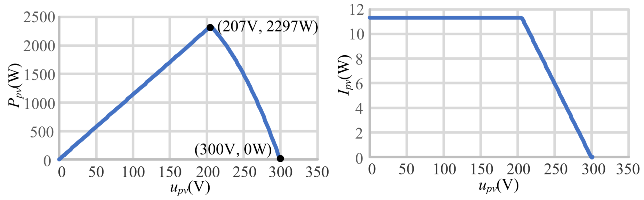

(a) (b)

Fig. 36. Emulated characteristics of the PV array in Chroma 62100H-600S. (a) *P-V* curve of emulated PV array. (b) *I-V* curve of emulated PV array.

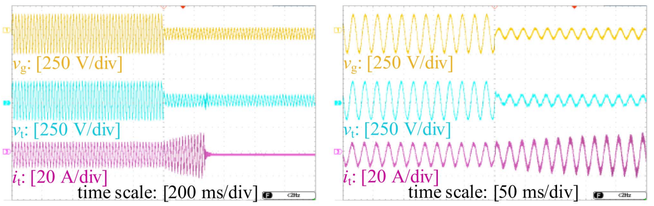

(a) (b)

Fig. 37. Results of GFL inverter with traditional control when V_g drops to 0.2 p.u. (a) GFL inverter loses stability. (b) Zoomed in view.

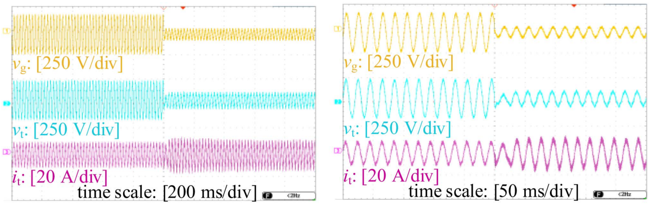

(a) (b)

Fig. 38. Results of GFL inverter with enhanced control when V_g drops to 0.2 p.u. (a) GFL inverter keeps stable. (b) Zoomed in view.

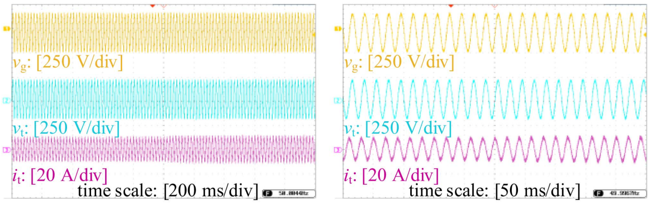

(a) (b)

Fig. 39. Results of GFL inverter with enhanced control when output power of PV increases from 1500 to 1700 W. (a) Dynamics of voltage and current. (b) Zoomed in view.

enhanced control, the overshoot of grid current is 12%, the GFL inverter can operate normally and restore stability within 0.2 s, as depicted in Fig. 38. When the input PV power varies, the GFL inverter with the enhanced control performs well. As shown in Fig. 39, when the power reference of the PV array increases from 1500 to 1700 W, the PV array output voltage is 242 V. The grid current and voltage of the GFL inverter still remains stable. The experimental results prove that the enhanced control can improve the stability of the GFL inverter.

The experimental results of the GFM inverter are shown in Figs. 40–42. The grid current THD is 2.86%. When the grid voltage drops to 0.2 p.u., the GFM inverter triggers the current saturation and loses the stability, as shown in Fig. 40. The inverter is quickly blocked due to the protection. After applying the enhanced control, the overshoot of grid current is 26% and the GFM inverter recovers stable within 0.5 s, as depicted in Fig. 41. When the input PV power varies, the GFM inverter with the enhanced control can keep stable. As shown in Fig. 42, the power reference of the PV array increases from 1500 to 1700 W, the PV array output voltage is 242 V. The grid current and voltage of the GFM inverter still remains stable. The experimental results show that the enhanced control can effectively improve the stability of the GFM inverter.

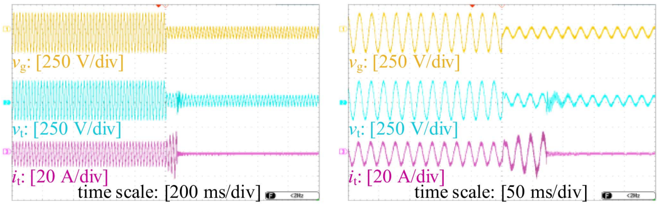

(a) (b)

Fig. 40. Results of GFM inverter with traditional control when V_g drops to 0.2 p.u. (a) GFM inverter loses stability. (b) Zoomed in view.

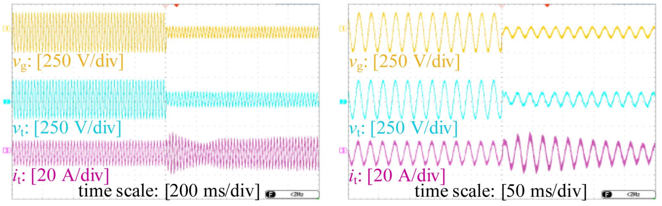

(a) (b)

Fig. 41. Results of GFM inverter with enhanced control when V_g drops to 0.2 p.u. (a) GFM inverter keeps stable. (b) Zoomed in view.

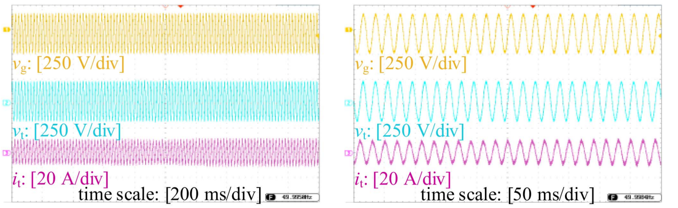

(a) (b)

Fig. 42. Results of GFM inverter with enhanced control when output power of PV increases from 1500 to 1700 W. (a) Dynamics of voltage and current. (b) Zoomed in view.

VI. CONCLUSION

The article analyzes the transient stability of the GFL inverter and the GFM inverter with considering the influence of the dc-link voltage dynamics. Then, the enhanced controls of the GFL inverter and the GFM inverter are proposed. The simulation results and the experimental results are given to verify the effectiveness of theoretical analysis and the enhanced controls. Conclusions are drawn as follows.

1) The GFL inverter is more prone to be constrained by its capacity and cannot output the active power. The active power of the GFL inverter is limited when the power angle is very small, while the active power of the GFM inverter is limited when the power angle is large.
2) The dc-link voltage dynamics increase the active power reference. It increases the acceleration area and reduces the maximum deceleration area for the GFL inverter and the GFM inverter. For the GFL inverter and the GFM inverter, a fast dc-link voltage response endangers the transient stability.
3) The equivalent elasticity is introduced in the enhanced control by analogy with the mass-spring-damper system. The transient stability of the power reserve control is enhanced by regulating the output active power of the PV source.

REFERENCES

[1] E. I. Batzelis, G. E. Kampitsis, and S. A. Papathanassiou, “Power reserves control for PV systems with real-time MPP estimation via curve fitting,” *IEEE Trans. Sustain. Energy*, vol. 8, no. 3, pp. 1269–1280, Jul. 2017.

[2] A. Sangwongwanich, Y. Yang, and F. Blaabjerg, “A sensorless power reserve control strategy for two-stage grid-connected PV systems,” *IEEE Trans. Power Electron.*, vol. 32, no. 11, pp. 8559–8569, Nov. 2017.

[3] A. Narang et al., “Dynamic reserve power point tracking in grid-connected photovoltaic power plants,” *IEEE Trans. Power Electron.*, vol. 38, no. 5, pp. 5939–5951, May 2023.

[4] Q. Peng, Z. Tang, Y. Yang, T. Liu, and F. Blaabjerg, “Event-triggering virtual inertia control of PV systems with power reserve,” *IEEE Trans. Ind. Appl.*, vol. 57, no. 4, pp. 4059–4070, Jul./Aug. 2021.

[5] H. D. Tafti, Q. Wang, C. D. Townsend, J. Pou, and G. Konstantinou, “Global flexible power point tracking in photovoltaic systems under partial shading conditions,” *IEEE Trans. Power Electron.*, vol. 37, no. 9, pp. 11332–11341, Sep. 2022.

[6] Y. Zhu, H. Wen, Q. Bu, X. Wang, Y. Hu, and G. Chen, “An improved photovoltaic power reserve control with rapid real-time available power estimation and drift avoidance,” *IEEE Trans. Ind. Electron.*, vol. 70, no. 11, pp. 11287–11298, Nov. 2023.

[7] M. G. Taul, C. Wu, S. -F. Chou, and F. Blaabjerg, “Optimal controller design for transient stability enhancement of grid-following converters under weak-grid conditions,” *IEEE Trans. Power Electron.*, vol. 36, no. 9, pp. 10251–10264, Sep. 2021.

[8] C. Shen, W. Gu, W. Sheng, and K. Liu, “Transient stability analysis and design of VSGs with different DC-link voltage controllers,” *CSEE J. Power Energy Syst.*, vol. 10, no. 2, pp. 593–604, Mar. 2024.

[9] M. G. Taul, X. Wang, P. Davari, and F. Blaabjerg, “An overview of assessment methods for synchronization stability of grid-connected converters under severe symmetrical grid faults,” *IEEE Trans. Power Electron.*, vol. 34, no. 10, pp. 9655–9670, Oct. 2019.

[10] “1,200 MW fault induced solar photovoltaic resource interruption disturbance report – Southern California 8/16/2016 event,” NERC, Jun. 2017. [Online]. Available: www.nerc.com

[11] “Odessa disturbance,” Joint NERC and Texas RE Staff Report, Sep. 2021. [Online]. Available: https://www.nerc.com/pa/rrm/ea/

[12] X. He, C. He, S. Pan, H. Geng, and F. Liu, “Synchronization instability of inverter-based generation during asymmetrical grid faults,” *IEEE Trans. Power Syst.*, vol. 37, no. 2, pp. 1018–1031, Mar. 2022.

[13] L. Fan, Z. Wang, and Z. Miao, “Large angle deviation in grid-following IBRs upon grid voltage dip,” *IEEE Trans. Energy Convers.*, vol. 39, no. 1, pp. 368–378, Mar. 2024.

[14] J. Zhao, M. Huang, and X. Zha, “Transient stability analysis of grid-connected VSIs via PLL interaction,” in *Proc. IEEE Int. Power Electron. Appl. Conf. Expo.*, 2018, pp. 1–6.

[15] H. Wu and X. Wang, “An adaptive phase-locked loop for the transient stability enhancement of grid-connected voltage source converters,” in *Proc. IEEE Energy Convers. Congr. Expo.*, 2018, pp. 5892–5898.

[16] Q. Hu, L. Fu, F. Ma, and F. Ji, “Large signal synchronizing instability of PLL-based VSC connected to weak AC grid,” *IEEE Trans. Power Syst.*, vol. 34, no. 4, pp. 3220–3229, Jul. 2019.

[17] X. Fu et al., “Large-signal stability of grid-forming and grid-following controls in voltage source converter: A comparative study,” *IEEE Trans. Power Electron.*, vol. 36, no. 7, pp. 7832–7840, Jul. 2021.

[18] X. Li, Z. Tian, X. Zha, P. Sun, Y. Hu, and M. Huang, “An iterative equal area criterion for transient stability analysis of grid-tied converter systems with varying damping,” *IEEE Trans. Power Syst.*, vol. 39, no. 1, pp. 1771–1784, Jan. 2024.

[19] Z. Shuai, C. Shen, X. Liu, Z. Li, and Z. J. Shen, “Transient angle stability of virtual synchronous generators using Lyapunov’s direct method,” *IEEE Trans. Smart Grid*, vol. 10, no. 4, pp. 4648–4661, Jul. 2019.

[20] J. Zhao, M. Huang, H. Yan, C. K. Tse, and X. Zha, “Nonlinear and transient stability analysis of phase-locked loops in grid-connected converters,” *IEEE Trans. Power Electron.*, vol. 36, no. 1, pp. 1018–1029, Jan. 2021.

[21] Y. Liu et al., “Transient stability enhancement control strategy based on improved PLL for grid connected VSC during severe grid fault,” *IEEE Trans. Energy Convers.*, vol. 36, no. 1, pp. 218–229, Mar. 2021.

[22] P. Yu, X. Zha, Z. Tian, P. Zhong, J. Sun, and M. Huang, “Frequency-dependent network analysis and stability enhanced design for voltage-source converters under weak grid conditions,” *IEEE Trans. Power Del.*, vol. 37, no. 6, pp. 4593–4602, Dec. 2022.

[23] X. He, H. Geng, J. Xi, and J. M. Guerrero, “Resynchronization analysis and improvement of grid-connected VSCs during grid faults,” *IEEE J. Emerg. Sel. Topics Power Electron.*, vol. 9, no. 1, pp. 438–450, Feb. 2021.

[24] H. Wu and X. Wang, “Design-oriented transient stability analysis of PLL-synchronized voltage-source converters,” *IEEE Trans. Power Electron.*, vol. 35, no. 4, pp. 3573–3589, Apr. 2020.

[25] X. Xiong, C. Wu, B. Hu, D. Pan, and F. Blaabjerg, “Transient damping method for improving the synchronization stability of virtual synchronous generators,” *IEEE Trans. Power Electron.*, vol. 36, no. 7, pp. 7820–7831, Jul. 2021.

[26] P. Ge, C. Tu, F. Xiao, Q. Guo, and J. Gao, “Design-oriented analysis and transient stability enhancement control for a virtual synchronous generator,” *IEEE Trans. Ind. Electron.*, vol. 70, no. 3, pp. 2675–2684, Mar. 2023.

[27] S. Sang, C. Zhang, X. Cai, M. Molinas, J. Zhang, and F. Rao, “Control of a type-IV wind turbine with the capability of robust grid-synchronization and inertial response for weak grid stable operation,” *IEEE Access*, vol. 7, pp. 58553–58569, 2019.

[28] Y. Guo, L. Chen, K. Li, T. Zheng, and S. Mei, “A novel control strategy for stand-alone photovoltaic system based on virtual synchronous generator,” in *Proc. IEEE Power Energy Soc. Gen. Meeting*, 2016, pp. 1–5.

[29] *Technical requirements for connecting photovoltaic power station to power system*, Standardization Administration of the People’s Republic of China, Standard GB/T 19964-2024, Mar. 2024, pp. 1–13. [Online]. Available: https://openstd.samr.gov.cn/bzgk/gb/newGbInfo?hcno=40D8691DFD7EC3CBA423CCBA65D262F3

[30] D. Pan, X. Wang, F. Liu, and R. Shi, “Transient stability of voltage-source converters with grid-forming control: A design-oriented study,” *IEEE J. Emerg. Sel. Topics Power Electron.*, vol. 8, no. 2, pp. 1019–1033, Jun. 2020.

[31] D. Wu, G. Li, M. Javadi, A. M. Malyscheff, M. Hong, and J. N. Jiang, “Assessing impact of renewable energy integration on system strength using site-dependent short circuit ratio,” *IEEE Trans. Sustain. Energy*, vol. 9, no. 3, pp. 1072–1080, Jul. 2018.

[32] *Testing specification for photovoltaic grid-connected inverter*, Standardization Administration of the People’s Republic of China, Standard GB/T 37409-2019, May 2019, pp. 1–33. [Online]. Available: https://openstd.samr.gov.cn/bzgk/gb/newGbInfo?hcno=8A25A04286515F893EF148E2D5078913

Yangjian Ling was born in Ganzhou, China, in 1997. He received the B.Eng. degree in electrical engineering from Northeastern University, Shenyang, China, in 2021. He is currently working toward the Ph.D. degree in electrical engineering with the School of Electrical Engineering and Automation, Wuhan University, Wuhan, China.

His current research interests include the modeling, transient stability, and control of grid-tied converter.

Meng Huang (Member, IEEE) received the B.Eng. and M.Eng. degrees in electronic science and technology from the Huazhong University of Science and Technology, Wuhan, China, in 2006 and 2008, respectively, and the Ph.D. degree in electrical engineering from The Hong Kong Polytechnic University, Hong Kong, 2013.

He is currently a Professor with the School of Electrical Engineering and Automation, Wuhan University, Wuhan. His research interests include the safe operation and control of grid-connected systems.

He was recipient of the Best Paper Award of the IEEE Transactions on Power Electronics in 2016, and the Excellent Paper Award of *CSEE Journal of Power and Energy System* in 2020. He is an Editor of *International Journal of Circuit Theory and Applications*, was Guest Editor of IEEE Journal of Emerging and Selected Topics of Circuits and Systems, Guest Associate Editor of IEEE Transactions on Industrial Applications and IEEE Journal of Emerging and Selected Topics of Power Electronics.

Pan Feng was born in Xingtai, China, in 2002. He received the B.Eng. degree in electrical engineering from Sichuan University, Chengdu, China, in 2023. He is currently working toward the M.S. degree in electrical engineering with Wuhan University. Wuhan, China.

His research interests include the modeling and stability analysis of virtual synchronous generator-based and dc-link voltage-synchronized-based grid-forming converters.

Minxuan Peng (Graduate Student Member, IEEE) was born in Chongqing City, China, in 2000. He received the B.S. degree in electrical engineering in 2021 from Wuhan University, Wuhan, China, where he is currently working toward the Ph.D. degree in electrical engineering.

His main research interests include topology and control of power electronic converters, and photovoltaic grid-connection.

Zhen Tian (Member, IEEE) received the B.S. degree in electrical engineering from Wuhan University, Wuhan, China, in 2014, and the Ph.D. degree in control science and engineering from Shanghai Jiao Tong University, Shanghai, China, in 2019.

During 2017–2019, he was a visiting scholar with the Department of Electrical and Computer Engineering, Illinois Institute of Technology, Chicago, USA. He has been with the School of Electrical Engineering and Automation, Wuhan University, since 2019, where he is currently an Associate Professor. His research interests mainly include modeling, control, and stability analysis of renewable energy generation, microgrid, and power-electronics-enabled power systems.

Sirui Shu received the B.S. and M.S. degrees in electrical engineering from Xi’an Jiaotong University, Xi’an, China, in 2019 and 2022, respectively. She is currently working toward the Ph.D. degree in civil engineering with Wuhan University, Wuhan, China.

She is currently an Engineer with State Grid Hubei Economic Research Institute, Wuhan, China. Her research interests include the modeling and control of converters-based renewable energy integration system.

Xiaoming Zha (Senior Member, IEEE) was born in Huaining, China, in 1967. He received B.S., M.S., and Ph.D. degrees in electrical engineering from Wuhan University, Wuhan, China, in 1989, 1992, and 2001, respectively.

He was a Postdoctoral Fellow with the University of Alberta, Canada, from 2001 to 2003. He has been a Faculty Member of Wuhan University since 1992, and became a Professor in 2003. He is currently the Deputy Dean with the School of Electrical Engineering, Wuhan University, Wuhan, China. His research interests include power electronic converter, the application of power electronics in smart grid and renewable energy generation, the analysis and control of microgrid, the analysis and control of power quality, and frequency control of high- voltage high-power electric motors.

Xin Ma received the bachelor’s and master’s degrees in electrical engineering from Zhejiang University, Hangzhou, China, in 2012 and 2016, respectively.

He is currently an Engineer with the Electric Power Research Institute, State Grid Ningxia Electric Power Company Ltd., Nanjing, China. His research interests include simulation and calculation of power system security and stability.